ADVANCED ENERGY MATERIALS
www.advenergymat.de

How Solvation Energetics Dampen the Hydrogen Evolution Reaction to Maximize Zinc Anode Stability

*Kingshuk Roy, Ashutosh Rana, Tushar K Ghosh, Joseph N Heil, Sayan Roy, Kathryn J Vannoy, Brian M. Tackett, Ming Chen, and Jeffrey E. Dick**

Aqueous zinc metal batteries (AZMB) are emerging as a promising alternative to the prevailing existing Lithium-ion battery technology. However, the development of AZMBs is hindered due to challenges including dendrite formation, hydrogen evolution reaction (HER), and ZnO passivation on the anode. Here, a tetraalkylsulfonamide (TAS) additive for suppressing HER, dendrite formation, and enhancing cyclability is rationally designed. Only 1 mM TAS is found that can effectively displace water molecules from the Zn^{2+} solvation shell, thereby altering the solvation matrix of Zn^{2+} and disrupting the hydrogen bond network of free water, as demonstrated through ^{67} Zn and ^{1}H nuclear magnetic resonance spectroscopy, high-resolution mass spectrometry (HRMS), and density functional theory (DFT) studies. Voltammetry synchronized with in situ monitoring of the electrode surface reveals suppressed dendritic growth and HER in the presence of TAS. Electrochemical mass spectrometry (ECMS) captures real-time HER suppression during Zn electrodeposition, revealing the ability of TAS to suppress the HER by an order of magnitude. A ≈25-fold cycle life improvement from ≈100 h to over 2500 h in coin cells cycled in the presence of TAS. Furthermore, by suppressing passivation product formation, it is demonstrated that strategy robustly maximizes the stability of Zn metal anodes.

1. Introduction

In recent times, lithium-ion batteries have emerged as the most promising and widely used electrochemical energy storage devices.[1,2] However, these state-of-the-art battery chemistries suffer from several drawbacks stemming from the high cost of lithium and safety issues pertaining to the low flash point of the organic electrolytes used for Li-ion batteries.[3] This opens new avenues of inquiry beyond Li-based systems like Li/Na metal batteries, solid-state batteries, and Zn ion/metal batteries. Out of these, aqueous Zn metal batteries (AZMB) with Zn metal as the anode emerges as a beacon of advanced energy storage devices for mainly stationary storage, harnessing abundant Zn, cost-effectiveness, and a theoretical capacity of 820 mAh g^{-1}, 5854 mAh cm^{-3} of metallic Zn, low redox potential (−0.76 V vs the standard hydrogen electrode), cost-effectiveness, water compatibility, and inherent safety.[4–6] Most researched AZMBs involve the use of mildly acidic aqueous electrolytes (pH range of 3–7).[7,8] Despite the advantages of AZMBs, there are several challenges, like the intrinsic thermodynamic instability of the Zn metal anode in mildly acidic electrolytes, which triggers the hydrogen evolution reaction (HER), Zn corrosion, and dendritic growth, that impede the development and commercialization of Zn battery chemistry.[9–12]

The performance of AZMBs is plagued by the formation of dendrites and HER, which strongly correlates to the pH of the electrolyte. The most used electrolytes for AZMBs are mildly acidic (pH 4–7) in nature.[7,8] During the charging of an AZMB, Zn^{2+} ions migrate toward the surface of the electrode and the following reaction takes place; $Zn^{2+} + 2e^- \rightarrow Zn^0$, leading to the deposition of Zn^0. Prior to the electrodeposition, the solvation matrix around Zn^{2+} is lost, leading to the accumulation of desolvated water molecules in the vicinity of the electrode which takes part in other side reactions like HER. Along with electrodeposition, water-splitting reactions occur leading to the evolution of hydrogen gas. This process is significantly pronounced in mildly acidic electrolytes due to their low pH and thermodynamic reduction potential predicted by the Nernst equation.

K. Roy, A. Rana, T. K Ghosh, S. Roy, K. J Vannoy, M. Chen, J. E. Dick
Department of Chemistry
Purdue University
West Lafayette, IN 47907, USA
E-mail: jdick@purdue.edu
J. N Heil, B. M. Tackett
Davidson School of Chemical Engineering
Purdue University
West Lafayette, IN 47907, USA
J. E. Dick
Elmore Family School of Electrical and Computer Engineering
Purdue University
West Lafayette, IN 47907, USA

The ORCID identification number(s) for the author(s) of this article can be found under https://doi.org/10.1002/aenm.202303998

DOI: 10.1002/aenm.202303998

During charging, HER occurs by the following reaction: $2H_2O + 2e^- \rightarrow 2OH^- + H_2\uparrow$ and at rest: $Zn + 2H_2O \rightarrow Zn(OH)_2 + H_2(\uparrow)$.[5,6,13] Along with this, gas evolution may happen from the H^+ ions residing on the hydrogen bond network of "free" water molecules present in the solution due to the mildly acidic nature of the electrolyte.[13,14] Therefore, HER may happen from both solvated and free water molecules. In general, HER triggers a localized accumulation of hydroxide ions (OH^-), leading to Zn corrosion, the formation of a zinc oxide (ZnO) passivation layer ($Zn + 2OH^- \rightarrow Zn(OH)_2 + 2e^- \rightarrow ZnO + H_2O + 2e^-$).[7] This layer is insulating in nature and impedes the cyclability of the battery by increasing the overall cell resistance. Eventually, these processes culminate in the growth of Zn dendrites, spurred by the tip effect and uneven Zn^{2+} flux distribution.[7,10,11]

Various strategies have emerged to enhance the stability of Zn metal anodes, like surface coating, host material design, separator modification, and electrolyte optimization. Nonetheless, it is important to realize that the cathode comes with an altogether different set of problems, which is not the prime focus of the work. Notably, the electrolyte optimization approach has garnered recognition as a highly feasible and effective means to bolster the electrochemical performance of Zn anodes. In most works related to the approach of optimizing electrolytes for achieving high-performing AZMBs, the strategies commonly employed include the use of organic/inorganic additives, high-concentration electrolytes, and the addition of a co-solvent.[13–22] It is crucial to emphasize that these strategies often revolve around modulating the solvation energetics of Zn^{2+} in the electrolyte, interacting with the hydrogen bond network of free water in the electrolyte, and adsorption of molecules to the Zn^0 electrode surface to suppress corrosion. This work focuses on the utilization of a meticulously synthesized additive molecule to achieve ultra-stable zinc metal anodes, enhancing the performance of AZMB. Drawing from various reported works in the literature on the use of organic additive molecules, several key observations emerge concerning the AZMB system. First, the sluggish desolvation kinetics of coordinated Zn^{2+} ions play a crucial role in ensuring long-term stability.[18] Second, the preferential adsorption of additive molecules to the Zn^0 surface can suppress the activity of free water, thereby mitigating HER and side-product formation, consequently enhancing the stability of the zinc anode.[23] Last, certain additive molecules may interact and disrupt the H-bond network of free water, leading to reduced transport of H^+ to the electrode surface.[13] This disruption could potentially result in suppressed HER during electrodeposition, contributing to the enhancement of the long-term stability of the battery.

Herein, we detail the synthesis of an N, N-dimethyl, N′, N′-diethyl sulfonamide (tetra alkyl sulfonamide; TAS) organic additive for enhancing the stability of Zn metal anode in 2 M $ZnCl_2$ electrolyte. The synthesis of TAS follows a straightforward procedure (see Supporting Information page no. 4 for details), ensuring easy scalability (yield> 90%). Due to the hyperconjugation effect of four alkyl group and positive resonance effect of two nitrogen atoms (evident from the structure of TAS shown in Figure S1, Supporting Information), the overall electron density on the oxygen atoms high, thereby making the overall molecule extremely electronically rich. Leveraging this heightened electron-donating propensity, we demonstrate TAS's capability to replace water molecules within the Zn^{2+} ion solvation matrix, effectively disrupting the H-bond network of free water molecules. This effect is comprehensively illustrated through ^{67} Zn and ^{1}H nuclear magnetic resonance (NMR) spectroscopy, high-resolution mass spectrometry (HRMS), and DFT studies. With the use of time synchronized in situ optical microscopy coupled with voltammetry and electrochemical mass spectrometry (ECMS), we show real-time suppression of Zn dendrites and H_2 evolution (27.15 nmol vs 2.7 nmol) in the presence of only 1 mM TAS and supressed electron-transfer (ET) kinetics of zinc electrodeposition in the presence of TAS. Furthermore, we establish that the introduction of 1 mM TAS significantly extends the cycle life of zinc symmetric cells by an impressive factor of 20—from ≈100 h to ≈2500 h. It is essential to note that the amount of additive used in this work (1 mM) is significantly less compared to other reported additives for high-performing AZMBs.[12,24–36] The ratio of the stability of the Zn anode to the amount of additive used is one of the highest compared to other works reported in the literature.[26,27,12,28,32,36–40] Notably, the presence of TAS effectively curbs side product formation, fostering the generation of Zn^{2+} conducting species while suppressing Zn^{2+} insulating species like $Zn_5(OH)_8.Cl_2.H_2O$. Besides this, TAS proved to work extremely well with other counter anionic Zinc salts like Zinc sulfate and Zinc trifluoromethanesulfonate (Zinc triflate) in terms of effectively modulating solvation structure, giving rise to a very uniform and homogenous Zinc growth and thereby proving its ability to become a universal additive for high-performance aqueous Zinc metal batteries. In the absence of TAS, non-uniform, dendritic growth featuring void-containing Zn clusters prevails, while TAS introduction yields uniform, compact growth. The distinctive feature of this study lies in its insightful exploration of how a carefully crafted functional group moiety can significantly impact the modulation of the solvation matrix, regardless of the counter anion. Eventually, even a minute quantity of it proves to be highly effective in this aspect.

2. Results and Discussion

This section delves into the role of TAS as an electrolyte additive in 2 M $ZnCl_2$, effectively suppressing dendrite formation, corrosion, HER, and enhancing the cycle life of AZMB. First, the effect of the addition of TAS to the Zn^{2+} solvation matrix was examined using ^{67} Zn NMR, HRMS, and DFT. Employing a three-electrode setup, cyclic voltammetry (CV) and linear sweep voltammetry (LSV) analyses were conducted with an in situ monitoring of the working electrode. The exchange current density was calculated from the cathodic and anodic sweeps of CV using Tafel analysis based on the Butler–Volmer (BV) formulation. Furthermore, TAS's proficiency in HER suppression was demonstrated through electrochemical methods (LSV), ^{1}H NMR, ^{67} Zn NMR, ECMS, and DFT. To scrutinize the impact of TAS on the long-term coin cell stability, Zn symmetric cells and full cells were cycled. SEM and X-ray CT facilitated ex-situ post-cycling morphology analysis. Composition of SEI and side-product formation during coin cell cycling was assessed using XRD and XPS.

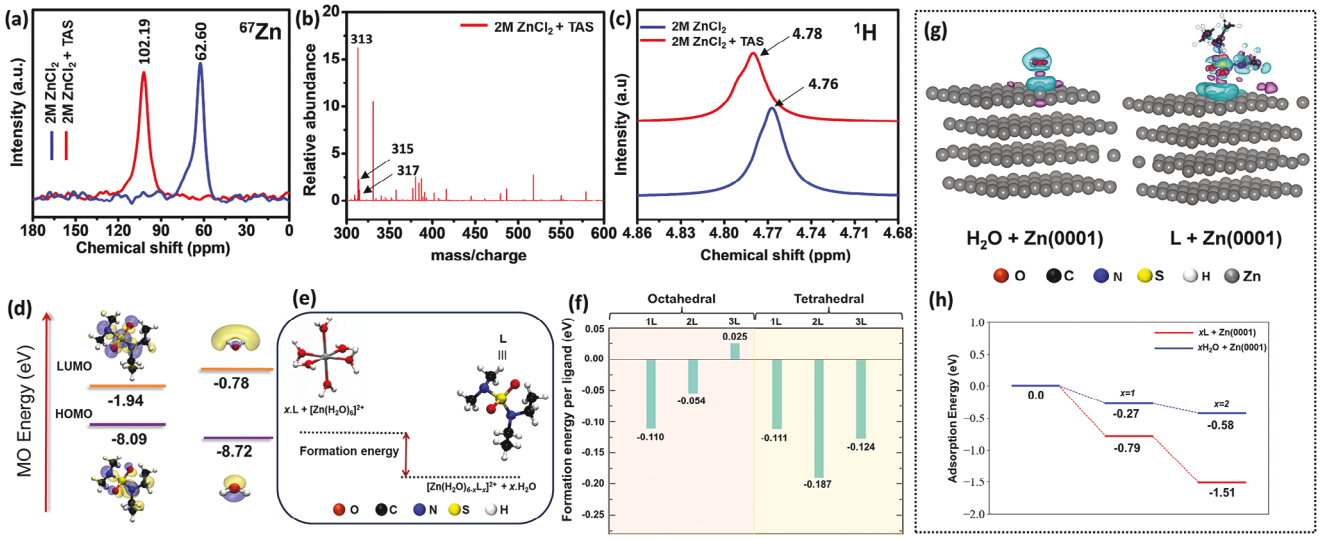

Figure 1. a) ^{67} Zn NMR for Aq. 2 M $ZnCl_2$ in the presence and absence of the tetraalkylsulfonamide (TAS) b) HRMS data of the Aq. 2 M $ZnCl_2$ with TAS c) ^{1}H NMR for Aq. 2 M $ZnCl_2$ in the presence and absence of TAS d) HOMO–LUMO calculation from DFT of the gas phase TAS and H_2O molecules e) Schematic representing the energetics associated with replacement of H_2O with TAS molecules in the Zn^{2+} solvation matrix taking octahedral geometry into consideration f) Calculation of formation free energies associated with the H_2O substitution by subsequent TAS additive addition to the system g) Adsorption of TAS and H_2O molecules on the Zn (0001) substrate from first principle calculations. The blue electron cloud represents the difference in electronic charge density, and h) Calculation on the adsorption energies associated with the adsorption of 1 or 2 molecules of TAS versus H_2O.

2.1. Solvation Structure of Zn^{2+}, Disruption of H-Bond Network and Interfacial Dynamics

Even with a tiny addition of 1 mM of TAS in the electrolyte, there is a notable shift in the ^{67} Zn chemical shift values as shown in **Figure 1a**. The chemical shift for Zn–H_2O–TAS is 102.9 ppm and for Zn–H_2O is 62.6 ppm, which indicates the deshielding effect of the solvation sheath on Zn^{2+}. Overall, this reveals that the addition of TAS in 2 M $ZnCl_2$ alters the solvation sheath of the Zn^{2+} complex in the electrolyte. To further inspect the effect of TAS on the Zn^{2+} solvation sheath, HRMS was performed. As displayed in Figure 1b, there are distinct signals from TAS containing $[Zn(H_2O)(OH)_3(TAS)]^-$ complexes at $m/z = 313$, 315 and 317. The different peak position and intensities for the same chemical structure are caused by the isotope pattern of Zn, including 48.6% abundance of Zn (64), 27.9% abundance of Zn (66), and 18.8% abundance of Zn (68). Both ^{67} Zn NMR spectroscopy and HRMS show preferential replacement of H_2O with TAS molecules. Intuitively, this occurs as TAS possesses dual N, N di-alkyl (-NR_2) groups, where R signifies alkyl groups. These groups enhance electron-donating capability in O atoms due to the positive resonance effect of —NR_2 groups. Consequently, TAS exhibits elevated Lewis basicity, enabling it to effectively displace water molecules within the Zn^{2+} solvation arrangement.

Another important aspect of the addition of TAS molecule in 2 M $ZnCl_2$ is to examine its effect on free H_2O molecules (free refers to H_2O molecules not involved in Zn^{2+} coordination) in the Aq. 2 M $ZnCl_2$ electrolyte. ^{1}H NMR spectroscopy (collected in a 500 MHz Bruker NMR spectrometer using MilliQ water as the solvent) reveals that the addition of TAS is associated with a larger chemical shift of 4.78 ppm versus 4.76 ppm in the absence of TAS, as shown in Figure 1c. In mildly acidic electrolytes like Aq. 2 M $ZnCl_2$ solution harbor a notable concentration of H^+ ions, predominantly localized within the hydrogen bond network of free water molecules.[41] A higher value of chemical shift in the presence of TAS is due to disruption of the H bond network leading to lower electron density of H atoms in water. An effective H-bond disruption in the presence of TAS can effectively inhibit HER as it can block and reduce the transport of H^+ and OH^- through the Grotthuss diffusion mechanism.[16,17,42,43] This effect is elaborated in the subsequent section.

The HOMO–LUMO energy level of the gas phase water and TAS molecule was calculated using DFT as shown in Figure 1d. TAS molecule exhibits a lower HOMO energy level versus H_2O molecule (−8.09 eV vs −8.72 eV, respectively). This difference of 0.63 eV shows that the TAS molecule exhibits an enhanced electron-donating capability (labile nature) versus H_2O molecules, indicating favorable replacement of H_2O with TAS molecules in the Zn^{+2} solvation sheath. We employed DFT calculation to check if the reaction is thermodynamically favorable in the forward direction. To examine this, the formation energy of Zn^{2+}–TAS bonded complexes (in the gas phase) was calculated (See Figure 1e,f). In the absence of any TAS molecule, Zn^{2+} complexes exist in an octahedral (OD) complex ($[Zn(H_2O)_6]^{2+}$) or a tetrahedral (TD) complex ($[Zn(H_2O)_4]^{2+}$). As shown in Figure 1e,f, the replacement of water molecules by TAS molecules (represented as L) into Zn^{2+} OD and TD complexes yields a favorable (negative) formation energy. The formation energy was calculated by the following equation:

$$\Delta E_f = E_{\left[Zn\left(H_2O\right)_{6-x}L_x\right]^{2+}} + x.E_{H_2O} - x.E_L - E_{\left[Zn\left(H_2O\right)_6\right]^{2+}} \quad (1)$$

Where, ΔE_f represents the formation energy, which was found to be negative for both TD and OD complexes, implying a spontaneous replacement of TAS molecules with H_2O. In the OD complexes, the formation energies per TAS molecules were

calculated to be −0.110, −0.054, and 0.025 eV (Figure 1f), respectively showing favorable replacement of two H_2O molecules with TAS molecules in OD complex leading to the formation of $[Zn(H_2O)_{6-x}(TAS)_x]^{2+}$ species in the electrolyte. The formation energy of TD complex was calculated with respect to OD complex. The replacement of successive H_2O molecules with TAS molecules in the TD complex yields formation energies of −0.111, −0.187, −0.124 eV (Figure 1f) respectively for 1, 2, 3 TAS molecules, respectively, to form $[Zn(H_2O)_{4-x}TAS_x]^{2+}$, complexes. Negative ΔE_f values of TD and OD complexes for replacement of one and two H_2O molecules suggest that replacement of H_2O with TAS molecules can be stabilized both in octahedral and tetrahedral geometries. However, based on Scheme S1 (Supporting Information), it can be clearly seen that when no TAS is added to the system, the system clearly wants to stay in the OD coordination and is rather unstable in the TD configuration. Furthermore, the Zn—TAS bond strength becomes weaker with each subsequent replacement of water molecules in the Zn solvation matrix. This is explained based on the Zn—TAS bond length (BL), after the addition of one TAS molecule BL was found to be 2.14Å, for two ligand replacement– 2.27 and 2.18Å, for insertion of third ligand molecule– 2.37, 2.16, and 2.15Å. Based on DFT calculation we believe, taken OD complexes into consideration that the exchange of more than two water molecules in an OD complex is less likely to happen which might be caused because of the severe steric hindrance originating from the additive.

Along with the favorable replacement of water molecules in the solvation matrix of Zn^{2+}, the interaction of the TAS molecule with the Zn surface was examined using DFT. Figure 1g shows the interaction of H_2O and TAS molecule with the Zn (0001) facet, where H_2O interacts with the surface by the O atom and the TAS molecule interacts simultaneously with O, H, and N center. The (0001) surface of Zn is frequently used in theoretical calculations for surface modeling[46] and employed in this study. Metallic Zn possesses a hexagonal $P6_3/mmc$ space group, with an energy above the hull of 0.00 eV/atom, indicating its most stable phase. Due to its intrinsic hexagonal close-packed (hcp) structure, Zn metal tends to adopt the (0001) Zn facet to minimize surface energy. The Zn atoms, on the (0001) plane, are arranged neatly in a regular hexagonal structure, creating a flat surface to minimize surface energy. This phenomenon has been observed in various experiments and theoretical calculations.[44–47]

In the absence of TAS, the BL of the Zn (0001)–O center (H_2O) was 2.44 *Å* whereas, for TAS there are multiple interaction sites as listed: i) two different O centers interacting with Zn (0001) surface with BL of 2.62 and 2.85 *Å*; ii) N center with Zn (0001)–N BL of 3.08 *Å*; and iii) H center with Zn (0001)–H BL of 3.1 *Å*. This is evident from the charge density difference plot illustrated in Figure 1g, indicating the transfer of charge between the surface and adsorbate molecules. The electron density, shown in blue in Figure 1g, denotes the transfer of charge from the ligand to the molecule to the Zn (0001) surface. This process of charge transfer is more favorable for TAS compared to H_2O because of the higher HOMO energy level of TAS versus H_2O gas phase molecule, resulting in a more stable complex formation with TAS. The stability of the complex is measured by the adsorption energy of the H_2O and TAS molecule on the Zn (0001) surface. Figure 1h describes the calculated adsorption energies of H_2O and TAS molecule with the Zn (0001) facet, which shows favorable adsorption of TAS over H_2O on the Zn (0001) facet. To calculate the strength of binding energy, we calculated the adsorption energy of TAS and H_2O based on the following equation:

$$E_{ads} = E_{surface+molecule} - E_{surface} - E_{molecule} \quad (2)$$

E_{ads} denotes the adsorption energy, where a more negative value indicates favorable adsorption. The addition of a single TAS versus water molecule on the Zn (0001) facet yields an adsorption energy of −0.79 and −0.31 eV, respectively, showing favorable adsorption of TAS over H_2O. The higher binding energy can be attributed to the favorable HOMO energy levels and multiple interaction sites of TAS. A similar trend in adsorption energy was observed with the addition of two TAS and water molecule on the Zn substate (−1.51 and −0.58 eV, respectively). Energetics of various configurations of adsorption are given in SI. Electrochemical double-layer capacitance measurements shown in Figure S2 (Supporting Information) further shed light on the adsorption process. The capacitance (C) values of the double layer were determined to be 4.5 and 3.8 μF in the presence and absence (P/A) of TAS. A higher value of C was observed due to the preferential adsorption of TAS molecules over H_2O molecules on the electrode surface. This result is further supported by polarizability (α) calculations using DFT where TAS exhibits a higher value of α compared to H_2O, 119.21. and 7.4 a.u., respectively. Overall, the preferential adsorption of TAS over H_2O on the Zn (0001) substrate will lead to a homogenized Zn^{2+} flux toward the electrode surface during electrodeposition and suppressing side reactions by reducing the activity of H_2O molecules by preventing its interaction with the zinc anode.

2.2. Electrochemical Measurements

A series of steps intricately characterize the process of Zn electrodeposition, as elucidated in Figure S3 (Supporting Information). The sequence unfolds as follows: i) Solvated Zn^{2+} ($[Zn(H_2O)_6]^{2+}$) migrates/diffuses from the bulk electrolyte toward the anode in response to an applied current or potential; ii) Upon traversing the outer Helmholtz layer (OHL), the solvation sheath around Zn^{2+} gradually dissipates (de-solvation of the solvated complex), giving rise to the emergence of bare Zn^{2+} within the inner Helmholtz layer (IHL); iii) The bare Zn^{2+} is adsorbed onto the electrode surface, facilitating the actual electron-transfer (ET) process ($Zn^{+2} + 2e^- \rightarrow Zn^0$).[48] Concurrently with step iii), there might be the decomposition of the solvent, anions, or additives, leading to the formation of the Solid Electrolyte Interphase (SEI) and other unwanted side reactions like HER. As established in the previous section, the addition of TAS in 2 M $ZnCl_2$ allows for the replacement of H_2O molecules in Zn^{2+} solvation sheath which can have profound effects on the desolvation kinetics, ET kinetics, HER, and morphology of the electrodeposited Zn, which is examined using CV, LSV and ECMS.

2.2.1. Cyclic Voltammetry and Tafel Analysis

CV was performed in a three-electrode configuration (see Figure S4, Supporting Information), with the homemade Cu disk electrode as the working electrode, zinc foil as the counter electrode,

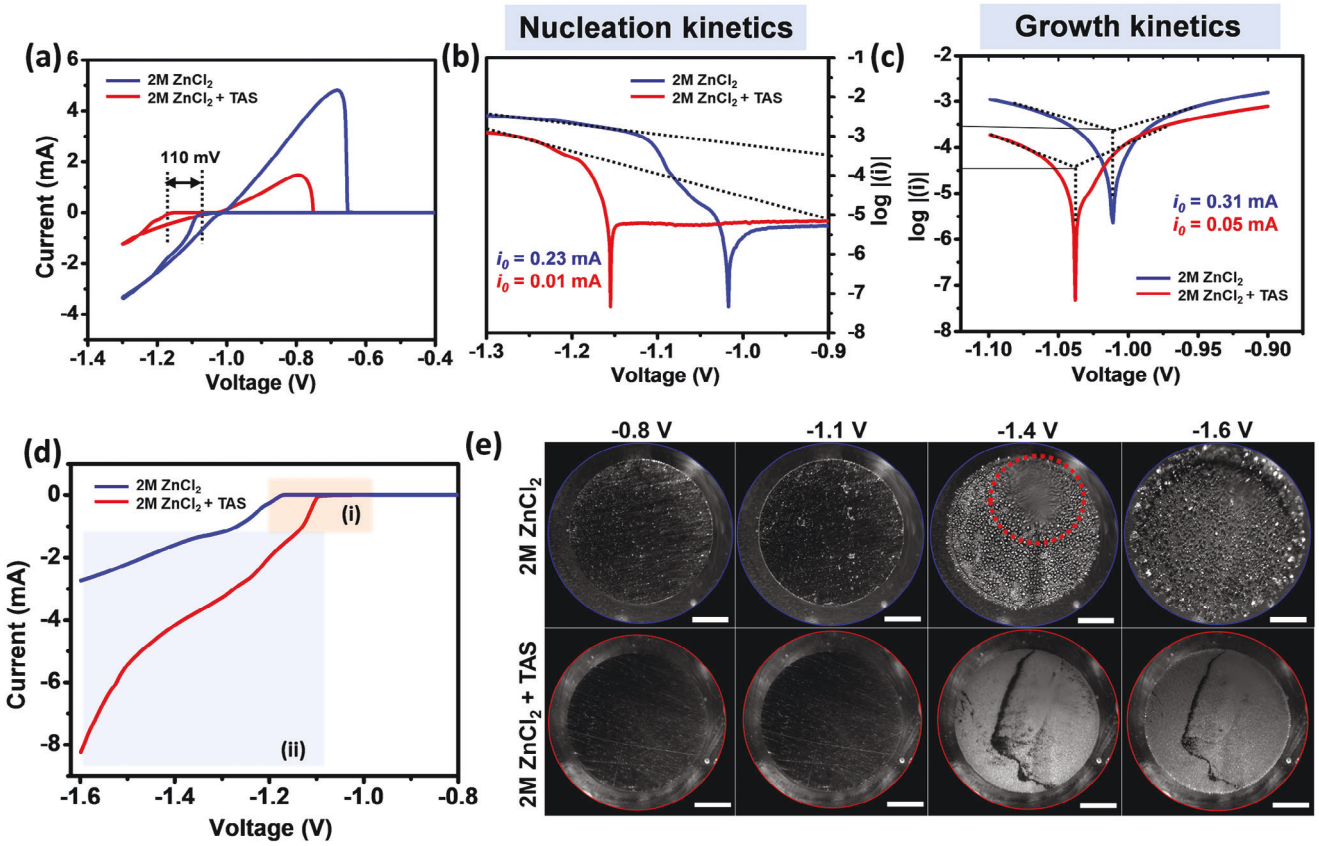

Figure 2. a) Cyclic voltammogram on a Cu macroelectrode in 2 M $ZnCl_2$ electrolyte in the P/A of the 1 mM tetraalkylsulfonamide (TAS) b,c) Tafel analysis depicting nucleation and growth kinetics translating directly from the cathodic and anodic sweep of CV d) Linear sweep voltammogram on the Cu macroelectrode using 2 M $ZnCl_2$ in the P/A of the 1 mM TAS e) In situ optical microscopy images acquired at different potential (−0.8, −1.1, −1.4, −1.6 V) during LSV in P/A of 1 mM TAS.

and Ag/AgCl in 1 M KCl serving as the reference electrode. **Figure 2a** illustrates the voltammogram acquired during the potential scan of the Cu disk, starting from an initial potential (E_i) of −0.45 V and sweeping to −1.25 V (cathodic sweep) before returning to E_i (anodic sweep), all carried out at a scan rate of 0.02 V s^{-1}. In the absence of TAS, the initial nucleation takes place at −1.1 V. However, in the presence of TAS, this value shifts to a more negative −1.2 V during the cathodic sweep. This variation of ≈125 mV in the nucleation overpotential indicates a deceleration in ET kinetics of Zn nucleation on the Cu surface in the presence of TAS.[23] During the anodic sweep, the juncture where the shift from zinc plating to stripping takes place is remarkably close in both scenarios—absence and presence of TAS—with potentials of −1.03 and −1.01 V, respectively. This similarity in transition potentials is unsurprising, given that the stripping action pertains to the surface of the electrodeposited zinc and remains unaffected by the additive's presence. However, noteworthy disparities arise in the curvature of the current response due to variations in ET kinetics in the two settings.[49] Moreover, the peak current exhibited during stripping diverged significantly between the P/A of TAS, measuring 1.5 and 4.8 mA respectively. Furthermore, the overall current within the system experiences a noteworthy reduction during both the cathodic and anodic sweeps when TAS is present. This reduction indicates an elevated system resistance resulting from the sluggish kinetics of ET during electrodeposition.

To delve deeper into the intricacies of zinc nucleation and growth, Tafel analysis was performed on the voltammogram shown in Figure 2a. Figure 2b illustrates the resulting Tafel plot originating from the cathodic sweep depicted in Figure 2a, elucidating the kinetics associated with Zn nucleation on the Cu surface.[23] The calculated exchange current (i_0) in the P/A of TAS in a 2 M $ZnCl_2$ solution was calculated from the y-intercept as 0.05 and 0.31 mA, respectively. Similarly, an additional Tafel plot was derived from the anodic sweep, showing the kinetics associated with Zn growth (see Figure 2c). Here again, the calculated exchange current for both the P/A of TAS in the 2 M $ZnCl_2$ solution was determined as 0.05 and 0.31 mA, respectively. The ET kinetics probed through voltammetry and Tafel analysis emerge as a convolution of the de-solvation of the solvated zinc complex and the actual ET.[49] The lower i_0 values extracted from both the cathodic and anodic sweeps (Figure 2b,c) serve as indicators of sluggish ET kinetics and subdued side reactions facilitated by the presence of 1 mM TAS in 2 M $ZnCl_2$.[50] Alongside, it is important to note that the TAS additive demonstrated an impressive efficacy when used in conjunction with alternative anionic Zinc salts such as Zinc sulfate and Zinc trifluoromethanesulfonate (Zinc triflate). It effectively influenced the solvation structure, resulting

in a consistently even and homogeneous growth of Zinc. Figure S5 (Supporting Information) shows that in the presence of a TAS additive, both Zinc sulfate and Zinc triflate solution gives rise to a very homogenous and uniform Zinc growth, and from the corresponding LSV data, it is also evident that the current is significantly less in the presence of the additive which again proves the fact of uniform and less-dendritic Zinc electrodeposition. This performance underscores TAS's versatility as a universal additive for aqueous Zinc metal batteries.

2.2.2. In Situ Optical Microscopy and Linear Sweep Voltammetry

On a similar experimental setup as CV, time-synchronized in situ monitoring of the Cu disk electrode surface was coupled with voltammetry. The comprehensive experimental arrangement is depicted in Figure S4 (Supporting Information). A custom-made 0.5 mm diameter copper disk electrode was vertically positioned within a Teflon cell filled with the electrolyte (2 M $ZnCl_2$, both with and without TAS). The setup was equipped with a high-resolution camera positioned above the Teflon cell, facilitating real-time visualization of the exposed copper disk. Bright-field optical micrographs of the electrode surface are captured using reflectance mode and diffuse light illumination. LSV was performed from an initial potential of −0.8 V and sweeping down to −1.6 V, aimed at scrutinizing the morphology of electrodeposited zinc both in the P/A of 1 mM TAS in Aq. 2 M $ZnCl_2$. The corresponding voltammograms are shown in Figure 2d, where a noticeable surge in current magnitude accompanies the progression toward more negative potentials. This current escalation is linked to the increasing surface area of the electrode, attributed to non-uniform dendritic zinc deposition. Figure 2e shows a series of micrographs obtained at distinct voltage intervals during the cathodic sweep. For a comprehensive visual depiction of the evolving morphology of electrodeposited Zn concerning applied potential, refer to Movie S1 and Figure S2 (Supporting Information). In the absence of TAS, at −1.4 V, there is observable non-uniform growth, characterized by dendritic structures. This dendritic growth becomes more pronounced as the potential shifts to more negative values (as evident in the micrograph captured at −1.6 V in Figure 2e). In contrast, in the presence of TAS, the growth pattern becomes strikingly planar and non-dendritic across all cathodic potentials. The overall current magnitude recorded during LSV exhibits a significant reduction (for instance, 8.1 mA vs 2.8 mA at −1.6 V) in the presence of TAS. This reduction can be attributed to the uniform and homogeneous zinc deposition, resulting in lesser morphological evolution. Notably, both in the P/A of TAS, the edge effect is clear in the micrographs, where electrodeposition primarily occurs at the periphery of the Cu-disk electrode (Figure 2e). This phenomenon arises due to the fact that for planar electrodes at a junction with an in-plane insulator, such edge effects are expected based on the current distribution for systems where the ohmic resistance is comparable with the charge transfer resistance.[23] The morphology of electrodeposited zinc undergoes a continuous evolution, encompassing an increasing surface area during the cathodic sweep. The appearance of dendritic structures arises when the kinetics of electrodeposition shift from ET-controlled to mass transport (MT) controlled.[51] Within a typical voltammetry experiment, the initial exponential rise in current corresponds to EC control, while a subsequent peak or a steady-state signifies reactions governed solely by diffusion/ MT control. The exact transition from ET control to MT control is intricate and multifaceted. Consequently, Figure 2d can be divided into two distinct phases: a) initial nucleation (ET control), and b) uncontrolled dendritic growth (MT control). The kinetics of electrodeposition operate under ET control during the initial nucleation phase and then transition to diffusion control (MT control), driving uncontrolled dendritic growth. The heightened prominence of the second phase, uncontrolled dendritic growth, becomes more pronounced in the absence of TAS demonstrating the efficacy of TAS in effectively suppressing the formation of dendrites during the process of electrodeposition, leading a uniform, planar zinc deposits.

2.2.3. Quantifying the Extent of HER During Zn Electrodeposition

The morphological evolution is closely tied to the extent of the HER during the electrodeposition process.[13] Movie S1 (Supporting Information) vividly shows the occurrence of substantial HER (noticeable bubbling at the electrode surface) during electrodeposition without TAS. In contrast, such an effect is notably suppressed in the presence of TAS (Movie S2, Supporting Information). This distinction is also discernible (indicated by a dotted red circle) in the micrograph captured at −1.4 V in the absence of TAS in Figure 2e. As previously discussed, there exists a strong correlation between the HER and the morphology of the electrodeposited zinc. This behavior manifests in both the presence and absence of TAS, albeit with varying degrees of intensity. To precisely investigate and quantify the extent of HER suppression in the presence of TAS, ECMS was employed, which details quantification of HER during Zn electrodeposition.[52] ECMS methodology is detailed in the Supporting information (Supporting Information page no.3). Electrochemical measurements were performed on a 3-electrode setup, with the Cu disk electrode as the working electrode (area ≈0.196 cm^2), Pt wire as the counter electrode, and Ag/AgCl in saturated KCl serving as the reference electrode. Chronopotentiometry was performed under a reduction current density of 5 mA cm^{-2} for 600 s in the P/A of TAS in Aq. 2 M $ZnCl_2$. The resulting voltage-time plots are shown in Figure S6 (Supporting Information), where the voltage response is not smooth, primarily arising from non-uniform growth whereas, in the presence of TAS additive, the profile is uniform with a high plating overpotential (expected from voltammetry experiments) owing to a very uniform, compact growth morphology. The amount of evolved H_2 was intricately quantified through electrochemical mass spectrometry (ECMS). In this measurement, we employ the mass spectrometer calibration to enable the measurement of H_2 production under voltage or current biases. The configuration of the ECMS system enables the mass spectrometer to swiftly identify hydrogen or any gas species with a collection efficiency of 100% within a matter of seconds, surpassing the time resolution achieved by certain research groups employing Gas Chromatography (GC).[53–57] **Figure 3a** schematically details the mechanisms of the ECMS instrument where research purity helium (purity of 6N, obtained from A-OX Welding) was delivered via an internal mass flow controller as the carrier gas that played the role of maintaining the pressure gradient,

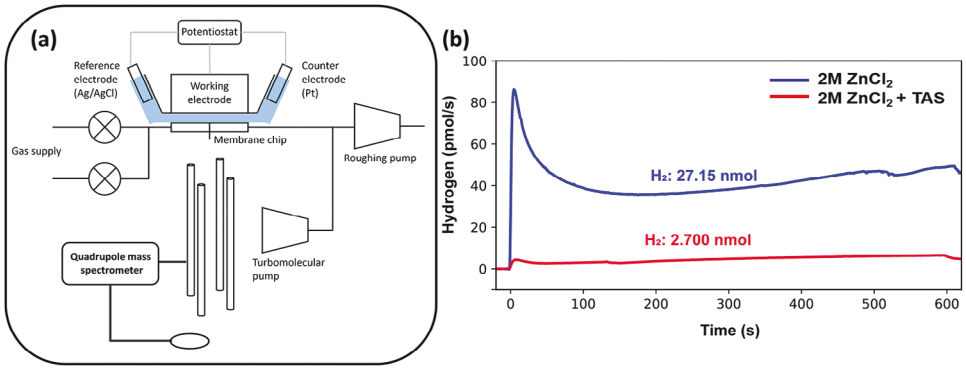

Figure 3. a) Schematic illustration of the working principle of the electrochemical mass spectrometer (ECMS) b) Real-time in situ quantification of the hydrogen gas evolved using 2 M $ZnCl_2$ in the P/A of the tetraalkylsulfonamide (TAS) additive.

facilitating the convection of gaseous species into the inlet of the mass spectrometer. The working electrode, composed of a Cu disk, the Ag/AgCl reference electrode immersed in 3.4 M KCl (provided by eDAQ), and the platinum (Pt) wire counter electrode, were all linked to a potentiostat (Biologic SP-300) under the control of the EC-Lab software. The valve and mass spectrometer control, as well as data collection, were managed using Zilien software (from Spectro Inlets). Ixdat Python package, specifically developed for Electrochemical Mass Spectrometry (ECMS) analysis, was employed for data processing.

Notably, in the presence of TAS, only 2.7 nmol of H_2 evolved, compared to the 27.15 nmol generated in its absence over the electrodeposition period (Figure 3b). This vividly underscores TAS's remarkable effectiveness in actively suppressing HER during electrodeposition. In fact, this proves that TAS is potent enough in tuning the solvation matrix and even a minute amount of additive can result in an order of magnitude decrease in the quantity of evolved H_2. The reduction of HER with the presence of TAS additive results in a uniform, dense SEI (in contrast to the 2 M $ZnCl_2$ case in the absence of TAS). The extent of side product formation and morphology of SEI is being discussed in paragraph 3.4 in detail. These conditions were chosen to closely mimic the operational parameters of coin cells or pouch cells, where a constant current mode is conventionally applied during battery cycling.

2.3. Long Term Cycling Stability of Zn Symmetric Cell in P/A of TAS

Based on voltammetry and ECMS, we realized that TAS enables uniform, non-dendritic Zn deposition and suppresses HER. However, in order to determine its applicability as a potential electrolyte additive for an AZMB for stabilizing the Zn metal anode, long term coin cell cycling was performed. The enhanced stability of the Zn anode in the presence of TAS was assessed by the cycle life of Zn symmetric cells. Symmetric coin cells were galvanostatically charged and discharged at a current of 1 mA cm^{-2} with a capacity of 0.5 mAh cm^{-2}. The voltage versus time profile in the P/A of TAS is shown in **Figure 4**. The addition of 1 mM TAS increases the cycle life of the symmetric cells by ≈20 times as compared to TAS-free Aq. 2 M $ZnCl_2$. The inset **(i)** of Figure 4 shows a nucleation overpotential (η_{nuc}) of 60 mV versus 20 mV in P/A of TAS. An increased value of nucleation overpotential is expected in the presence of TAS due to sluggish ET values (lower i_o values in the presence of TAS), as discussed within the voltammetry results. Moreover, these values of nucleation overpotential have a strong influence on the morphology of electrodeposited zinc. The critical radius ($r_{critical}$) of the deposited Zn nucleus is inversely proportional to η_{nuc}; $r_{critical} \propto 1/\eta_{nuc}$ and the density (A) is directly proportional to the cube of η_{nuc}; $A \propto \eta_{nuc}^3$.[58] Therefore, higher η_{nuc} values in presence of TAS leads to smaller $r_{critical}$ and higher A of the deposited Zn nucleus, leading to a uniform and non-dendritic deposition.[23,59]

Symmetric cells fabricated using 2 M $ZnCl_2$ with 1 mM TAS exhibit a stable cycle life of ≈2500 h., whereas in the absence of TAS, coin cells fail after 70–80 h. of cycling due to short circuit. This is evident from the inset **(ii)** of Figure 4 where, the current abruptly decreases and yields a flat voltage profile, characteristic of a short circuit. In inset **(ii)** of Figure 4, at 55 h of cycling, the cell softly shorts and starts functioning again at 60 h but eventually undergoes a permanent short circuit at ≈75 h of cycling. Once a flat voltage profile was observed after a permanent short circuit, the cycling of TAS free symmetric cell was stopped, decrimped, and the entire electrode–separator-electrode stack was subjected to X-ray CT. This was done to avoid any damage to the electrode microstructures that led to a short-circuit. The morphology assessed using X-ray CT is shown in inset **(ii)** of Figure 4. The CT images show the presence of physical attachments between the two electrodes, leading to a short circuit. Even after the failure of TAS free symmetric cells, the voltage profile of symmetric cells with TAS exhibits a stable voltage profile up to ≈2500 h, as shown in inset **(iii)** of Figure 4. In fact, when both the cells were stopped, the cell with 2 M $ZnCl_2$ is significantly swelled up (3.13 to 5.02 mm) whereas swelling to the one with the additive was much less (3.09 to 3.48 mm) (Figure S7, Supporting Information). This is absolutely in accordance with the ECMS data. Furthermore, Figure 4e shows rate performance data both in the presence and absence of the additive, where the symmetric cell was cycled with varying current densities ranging from 1, 3, 5, 8, 10, and 0.5 mA cm^{-2} to test the stability of the cell at very different applied current portfolios ranging from a low to high to low again current densities and it can be clearly seen that the cell where no additive was present failed at high current density eventually shorting the cell

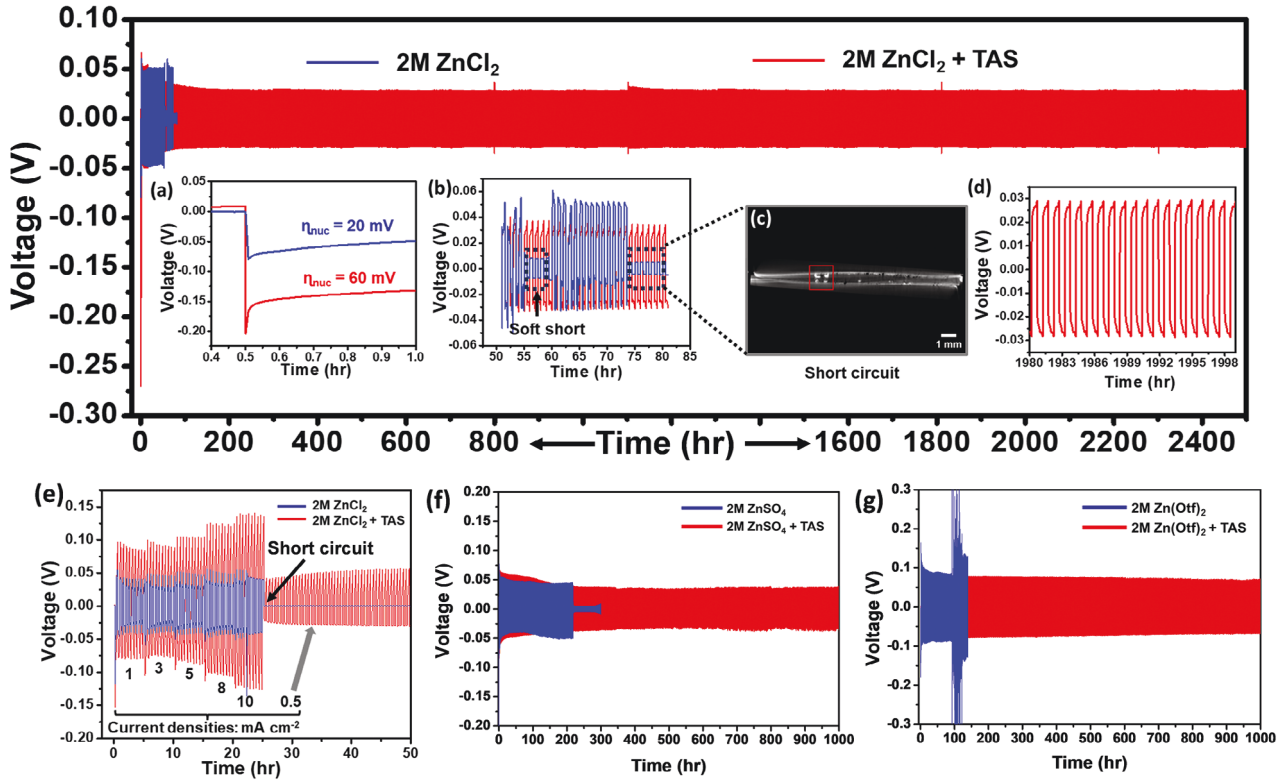

Figure 4. a–e) Symmetric cell cycling using 2 M $ZnCl_2$ electrolyte in the presence and absence of the TAS additive; inset (a) Initial electrodeposition showing nucleation overpotential difference b) Soft shoring followed by shorting of the cell with 2 M $ZnCl_2$ c) Post cycling X-ray CT data revealing the short-circuit d) Stable cycling profile of the 2 M $ZnCl_2$ cell with the presence of the TAS additive. e) Rate performance data at different applied current densities ranging from 1, 3, 5, 8, 10, 0.5 mA cm^{-2} f) Symmetric cell cycling stability data using 2 M $ZnSO_4$ electrolyte in the presence and absence of TAS additive g) Symmetric cell cycling stability data using 2 M $Zn(OTf)_2$ electrolyte in the presence and absence of TAS additive.

in contrary to the cell with the TAS additive whose stability was rock solid. In fact, we went one step further to fully understand the potential of the TAS additive to become a universal additive when different counter-anionic zinc salts were taken into consideration. Based on our understanding the thoughtful inclusion of tetra N-alkyl moieties should have been competent enough to tune the solvation matrix energetics irrespective of the counter anion and that is exactly what happened when it was being put to the test. Figure 4f,g showed the symmetric cell cyclic stability data using 2 M zinc sulfate ($ZnSO_4$) and 2 M zinc triflate ($Zn(OTf)_2$) electrolytes respectively in the presence and absence of the TAS additive. In both the cases, it can be clearly seen the addition of the TAS additive significantly improves the cycling stability compare to the salts themselves. This makes TAS an extremely versatile additive when it comes to tuning the solvation matrix energetics regardless of the counteranion. Moreover, to understand the practical applicability of the designed electrolyte additive, a full cell was fabricated using high-capacity V_2O_5 as the cathode and Zn metal as the anode. The full cell showed a reversible capacity of 370 mAh g^{-1} at an applied current density of 0.5 A g^{-1}. A charge–discharge stability of 100 cycles has been reported with ≈99.2% Coulombic efficiency (Figure S8, Supporting Information). Please refer to the Supporting Information page no. 2 for the fabrication process of the full cell. Overall, the anode stability (performance of Zn symmetric cell) reported in this work is very impressive compared to the additives reported in the literature for high-performing zinc metal batteries. Table S1 (Supporting Information) presents a comprehensive performance metric of the best electrolyte additives for ultra-stable zinc metal batteries. Evidently, from Table S1 (Supporting Information), TAS outperforms most of the additives reported in the literature, despite using only a tiny quantity of it. What distinguishes this work is the ratio of cycling stability to the amount of additives used. The distinctive feature of this study lies in its insightful exploration of how a carefully crafted functional group moiety can significantly impact the modulation of the solvation matrix, regardless of the counter anion. Eventually, even a minute quantity of it proves to be highly effective in this aspect. Figure S9 (Supporting Information) shows a comparison of the ratio of cycling stability to the amount of additives (for a normalized current density of 1 mA cm^{-2}), clearly demonstrating the effectiveness of TAS in stabilizing the zinc anode. Given the straightforward synthesis, low-cost precursor molecules, and scalability, we believe that TAS can be used to fabricate commercially relevant AZMBs.

2.4. Extent of Side Product Formation and Morphology of Deposited Zn in Symmetric Cell

Throughout the charge–discharge cycles of a battery, the surface of the anode can witness the decomposition of anions and solvents, leading to the formation of an SEI. The inherent

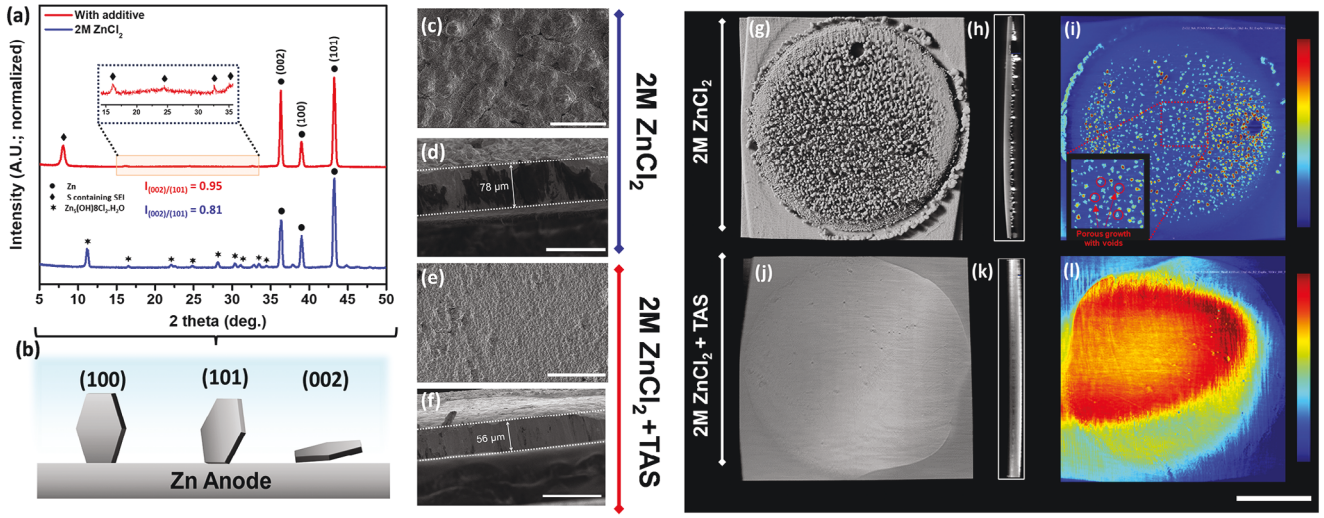

Figure 5. Post cycling characterizations a) X-ray diffraction data of Zn electrode cycled for 20 cycles at 1 mA cm^{-2} and a capacity of 1 mAh cm^{-2} in Aq. 2 M $ZnCl_2$ in P/A of 1 mM tetraalkylsulfonamide (TAS) b) Schematic for the different crystal facets associated with metallic zinc c) FESEM data of the symmetric cell cycled electrode for 2 M $ZnCl_2$ d) Cross-sectional FESEM data of the symmetric cell cycled electrode for 2 M $ZnCl_2$ e) FESEM data of the symmetric cell cycled electrode for 2 M $ZnCl_2$ with TAS additive f) Cross-sectional FESEM data of the symmetric cell cycled electrode for 2 M $ZnCl_2$ with TAS additive g–i) X-ray CT data of the electrodeposited Zn electrode with 2 M $ZnCl_2$ as the electrolyte j–l) X-ray CT data of the electrodeposited Zn electrode with 2 M $ZnCl_2$ with TAS additive as the electrolyte. The scale bar for (c)–(f) is 100 μm and for (g)–(l) is 4 mm.

composition, dynamic evolution, and stability of this SEI play a pivotal role in shaping the overall long-term cyclability of the battery.[60] To unravel the SEI's intricate composition on the Zn anode, comprehensive analyses were conducted, employing techniques such as XRD and XPS. As illustrated in **Figure 5a**, the XRD spectra exhibit distinctive features of the Zn metal anode, extracted from symmetric cells cycled over 20 plating/stripping cycles at a current density of 1 mA cm^{-2} and a capacity of 1 mAh cm^{-2}. Significantly, in the absence of TAS, insulating Zn^{2+} species resulted in the formation of $Zn_5(OH)_8.Cl_2.H_2O$ byproducts on the cycled electrode surface. Conversely, with the introduction of TAS, these undesired side reactions were obviously absent, highlighting TAS's effectiveness in suppressing their occurrence. Moreover, in the presence of TAS, a Zn^{2+} conductive S species-containing SEI layer emerged.[18] This is further confirmed by the post cycling XPS data (Figure S10, Supporting Information) wherein S2p, Cl2p, C1s, and O1s XPS spectra showed the formation of S-containing products in the SEI. S2p XPS spectra showed the formation of $ZnSO_4$ (19.5%), organic S-C species (29.5%), $ZnSO_3$ (42.1%) along with inorganic Zn–S species (8.9%). The C1s and O1s spectra also showed the formation of C–S (285.9 eV) and O–S (531.8 eV) respectively. Notably, such conductive Zn^{2+} entities were notably absent in the absence of TAS. The intricate relationship between SEI composition and the morphology of deposited zinc emerges as a recurrent theme. The propensity for Zn dendrite growth becomes more favorable as the angle between the Zn electrode surface and the growth direction increases.[61] This crystallographic orientation exerts a substantial influence on the growth direction, encompassing characteristics like surface texture and the nature of Zn deposits—ranging from non-uniform and dendritic to compact formations. Previous studies have underscored that Zn orientation indices such as (100), (101), and (002) correspond to angles of 90° (dendritic deposition), 30–70° (intermediate), and 0–30° (uniform, compact growth), respectively.[13] As a consequence, a heightened intensity of the (002) peak signifies more uniform and compact growth in contrast to other crystal facets. This relationship between crystallographic orientation and growth direction is summarized in Figure 5b. Upon analyzing Figure 5a, a noteworthy observation emerges: in the presence of TAS, both the intensity of (002) and (101) peaks are higher in the TAS-free case. The I (002)/ I (101) was determined to be 0.95 and 0.81 in P/A of TAS, respectively, which is consistent with the non-uniform, planar growth evidenced in voltammetry experiments when TAS is present. Conversely, no significant contrast in peak intensity was discernible for the (100) orientation in the presence of TAS.

To further understand the influence of an alteration in the coordination environment of Zn^{2+} on the surface texture of electrodeposited zinc, FESEM, and X-ray CT were performed on the electrodeposited Zn electrodes. In the absence of TAS (Figure 5c,d) the deposition is non-uniform and rough. Particularly evident in Figure 5d is the presence of dark-colored deposits, potentially indicating the formation of inactive Zn metal (dead zinc) generated during charge/discharge cycles. In contrast, when TAS is present (Figure 5e,f), the morphology is dense and smooth. The thickness of Zn deposits was measured at 56 and 78 μm in the P/A of TAS, respectively. in the plating/stripping cycle. This reduction in thickness attributed to TAS is ascribed to its role in promoting non-porous, compact growth. It has been previously been reported that there might be the formation of porous Zn deposits during charge–discharge cycles during to HER.[62] Given the significant HER reduction due to TAS, the porosity of the growth in P/A of TAS was examined of X-ray CT. Figure 5g–i and Figure S11 (Supporting Information) shows the CT images of the cycled Zn anode without TAS. Figure 5g,h clearly show non-uniform and dendritic growth, aligning with FESEM findings in the absence of TAS. Delving into detail, the contour plot in Figure 5i highlights the influence of significant

HER on Zn morphology. In the inset **(i)** of Figure 5i, a close-up reveals voids, and porous microstructures. These voids inside the electrodeposited Zn clusters are formed due to extensive HER in the absence of TAS. This prompts an intriguing question: could these voids trap evolved hydrogen gas, releasing it slowly? Figure S12 (Supporting Information) extends the mass spectrometry data from Figure 3b beyond the 600-second mark of applied current. Notably, a significant amount of evolved H_2 continues to register long after the current is halted, suggesting it is trapped within microstructures, eventually creating voids (which is consistent with our previous work). In contrast, TAS presence yields different outcomes. The growth becomes uniform, compact, and planar, as illustrated in Figure 5j–l and Figure S13 (Supporting Information), with void-free Zn deposits. Movies S3 and S4 (Supporting Information) show the zinc growth morphology evolution using 2 M $ZnCl_2$ electrolyte in the P/A of the TAS additive respectively.

3. Conclusion

In conclusion, this work provides a mechanism to rationally design an organic additive to maximize Zn anode stability. Using fundamental chemical knowledge, we designed the organic additive N, N-dimethyl, N′, N′-diethyl sulfonamide (TAS) and characterized its notable impact on enhancing the stability of Zn metal anodes in an Aq. 2 M $ZnCl_2$ electrolyte with only a very small amount (1 mM) of TAS. The labile nature of TAS versus H_2O facilitates the effective replacement of H_2O with TAS in the Zn^{2+} solvation matrix, resulting in improved reduction stability, suppressed dendrite growth, and reduced HER. These factors collectively influence ET kinetics, with sluggish kinetics observed and HER significantly suppressed in the presence of TAS. NMR, HRMS, and DFT showed that the additive is well-behaved in terms of complexation reaction, thereby reforming the solvation sheath. ECMS and in situ electrochemistry coupled optical microscopy probes real-time suppression of HER and mitigation of dendrite growth. Consequently, Zn symmetric cells exhibit an extended cycle life by a factor of 20, increasing from ≈100 to ≈2500 h in the presence of TAS. TAS also contributes to the formation of Zn^{2+} conductive decomposition products in the SEI layer, in contrast to the insulating Zn^{2+} decomposition products formed in its absence, leading to overall differences in cell voltage and dendrite growth tendencies, leading to a short-circuit. The presence of TAS fosters a desirable electrodeposited Zn morphology that is planar, compact, and non-dendritic, while its absence leads to heterogeneous growth with dendritic and void-containing Zn clusters. Alongside, the successful modulation of solvation structure for different counter anionic zinc salts and the achievement of uniform Zinc growth highlight TAS's potential to serve as a widely applicable performance-enhancing additive for aqueous Zinc battery technology. These findings and detailed mechanistic investigations forge a foundation for the rational design of powerful organic additives that can realize powerful new battery technologies.

Supporting Information

Supporting Information is available from the Wiley Online Library or from the author.

Acknowledgements

K.R, A.R., and J.E.D. acknowledge Austin Choi and Prof. Vilas Pol for their support in collecting the X-ray diffraction data. J.E.D. acknowledges Purdue University, the Sloan Foundation, and the National Science Foundation under grant CHE-2045672. T.K.G. and M.C. acknowledge support from Purdue startup funding. The authors acknowledge Alexandra Clark who assisted/acquired the images of cycled electrodes for this paper on a Zeiss Xradia 510 Versa 3D X-ray Microscope that was supported by the EVPRP Major Multi-User Equipment Program 2017 at Purdue University. The authors acknowledge Dr. John Harwood for helping recording nuclear magnetic resonance spectra at the Purdue University interdepartmental NMR facility.

Conflict of Interest

The authors declare no conflict of interest.

Author Contributions

K.R and A.R. contributed equally to this work. K.R., A.R., and J.E.D. wrote the manuscript. The concept of the additive and its subsequent impact on performance enhancement on Zinc metal anodes was conceived by K.R. All the electrolyte characterization, fundamental electrochemistry experiments, coin cell fabrication/ cycling, and post-cycling characterization were done by K.R and A.R. T.K.G. and M.C. performed the DFT calculations. J.N.H and B.M.T performed the ECMS measurements with experimental support by K.R. and A.R. S.R. synthesized the organic additive. K.J.V. prepared the table of contents graphic and contributed valuable experimental insight for the interpretation of data. K.R., A.R., and J.E.D. interpreted all data with necessary experimental and theoretical insight from all other co-authors. J.E.D. supervised all aspects of the work. All authors have agreed to the final version of the manuscript.

Data Availability Statement

The data that support the findings of this study are available from the corresponding author upon reasonable request.

Keywords

additive, electrochemical mass spectrometry, in situ electrochemistry, zinc battery

Received: November 22, 2023
Revised: January 13, 2024
Published online:

[1] H. Tian, P. Qin, K. Li, Z. Zhao, *J. Cleaner Prod.* **2020**, *261*, 120813.
[2] G. Harper, R. Sommerville, E. Kendrick, L. Driscoll, P. Slater, R. Stolkin, A. Walton, P. Christensen, O. Heidrich, S. Lambert, A. Abbott, K. Ryder, L. Gaines, P. Anderson, *Nature* **2019**, *575*, 75.
[3] H. Kim, J. Hong, K. Y. Park, H. Kim, S. W. Kim, K. Kang, *Chem. Rev.* **2014**, *114*, 11788.
[4] G. Feng, J. Guo, H. Tian, Z. Li, Y. Shi, X. Li, X. Yang, D. Mayerich, Y. Yang, X. Shan, *Adv. Energy Mater.* **2022**, *12*, 2103484.
[5] D. Han, C. Cui, K. Zhang, Z. Wang, J. Gao, Y. Guo, Z. Zhang, S. Wu, L. Yin, Z. Weng, F. Kang, Q. H. Yang, *Nat. Sustain.* **2022**, *5*, 205.
[6] L. Cao, D. Li, T. Pollard, T. Deng, B. Zhang, C. Yang, L. Chen, J. Vatamanu, E. Hu, M. J. Hourwitz, L. Ma, M. Ding, Q. Li, S. Hou, K. Gaskell, J. T. Fourkas, X. Q. Yang, K. Xu, O. Borodin, C. Wang, *Nat. Nanotechnol.* **2021**, *16*, 902.

[7] F. Yang, J. A. Yuwono, J. Hao, J. Long, L. Yuan, Y. Wang, S. Liu, Y. Fan, S. Zhao, K. Davey, Z. Guo, *Adv. Mater.* **2022**, *34*, 2206754.
[8] W. Fan, Z. Sun, Y. Yuan, X. Yuan, C. You, Q. Huang, J. Ye, L. Fu, V. Kondratiev, Y. Wu, *J Mater Chem A Mater* **2022**, *10*, 7645.
[9] H. Yang, Z. Chang, Y. Qiao, H. Deng, X. Mu, P. He, H. Zhou, *Angewandte Chemie – International Edition* **2020**, *59*, 9377.
[10] L. Kang, M. Cui, F. Jiang, Y. Gao, H. Luo, J. Liu, W. Liang, C. Zhi, *Adv. Energy Mater.* **2018**, *8*, 1801090.
[11] K. Zhao, C. Wang, Y. Yu, M. Yan, Q. Wei, P. He, Y. Dong, Z. Zhang, X. Wang, L. Mai, *Adv. Mater. Interfaces* **2018**, *5*, 1800848.
[12] P. Sun, L. Ma, W. Zhou, M. Qiu, Z. Wang, D. Chao, W. Mai, *Angewandte Chemie – International Edition* **2021**, *60*, 18247.
[13] L. Miao, Z. Guo, L. Jiao, *Energy Mater* **2023**, *3*, 300014.
[14] F. Wang, O. Borodin, T. Gao, X. Fan, W. Sun, F. Han, A. Faraone, J. A. Dura, K. Xu, C. Wang, *Nat. Mater.* **2018**, *17*, 543.
[15] J. Xie, Z. Liang, Y. C. Lu, *Nat. Mater.* **2020**, *19*, 1006.
[16] J. Cui, X. Liu, Y. Xie, K. Wu, Y. Wang, Y. Liu, J. Zhang, J. Yi, Y. Xia, *Mater. Today Energy* **2020**, *18*, 100563.
[17] Z. Su, J. Chen, J. Stansby, C. Jia, T. Zhao, J. Tang, Y. Fang, A. Rawal, J. Ho, C. Zhao, *Small* **2022**, *18*, 2201449.
[18] L. Cao, D. Li, E. Hu, J. Xu, T. Deng, L. Ma, Y. Wang, X. Q. Yang, C. Wang, *J. Am. Chem. Soc.* **2020**, *142*, 21404.
[19] W. Deng, Z. Xu, X. Wang, *Energy Storage Mater.* **2022**, *52*, 52.
[20] J. Wan, R. Wang, Z. Liu, L. Zhang, F. Liang, T. Zhou, S. Zhang, L. Zhang, Q. Lu, C. Zhang, Z. Guo, *ACS Nano* **2022**, *17*, 1610.
[21] T. C. Li, Y. Von Lim, X. L. Li, S. Luo, C. Lin, D. Fang, S. Xia, Y. Wang, H. Y. Yang, *Adv. Energy Mater.* **2022**, *12*, 2103231.
[22] Y. Zhong, Z. Cheng, H. Zhang, J. Li, D. Liu, Y. Liao, J. Meng, Y. Shen, Y. Huang, *Nano Energy* **2022**, *98*, 107220.
[23] A. Rana, A. Thakare, N. Kumar, B. Mukherjee, A. Torris, B. Das, S. Ogale, A. Banerjee, *ACS Appl. Mater. Interfaces* **2023**, *15*, 22781.
[24] J. Xu, W. Lv, W. Yang, Y. Jin, Q. Jin, B. Sun, Z. Zhang, T. Wang, L. Zheng, X. Shi, B. Sun, G. Wang, *ACS Nano* **2022**, *16*, 11392.
[25] B. Niu, Z. Li, D. Luo, X. Ma, Q. Yang, Y. E. Liu, X. Yu, X. He, Y. Qiao, X. Wang, *Energy Environ. Sci.* **2023**, *16*, 1662.
[26] N. Wang, X. Chen, H. Wan, B. Zhang, K. Guan, J. Yao, J. Ji, J. Li, Y. Gan, L. Lv, L. Tao, G. Ma, H. Wang, J. Zhang, H. Wang, *Adv. Funct. Mater.* **2023**, *33*, 2300795.
[27] J. Yang, Y. Zhang, Z. Li, X. Xu, X. Su, J. Lai, Y. Liu, K. Ding, L. Chen, Y. P. Cai, Q. Zheng, *Adv. Funct. Mater.* **2022**, *32*, 2209642.
[28] R. Yao, L. Qian, Y. Sui, G. Zhao, R. Guo, S. Hu, P. Liu, H. Zhu, F. Wang, C. Zhi, C. Yang, *Adv. Energy Mater.* **2022**, *12*, 2102780.
[29] M. Yan, N. Dong, X. Zhao, Y. Sun, H. Pan, *ACS Energy Lett.* **2021**, *6*, 3236.
[30] X. Xie, S. Liang, J. Gao, S. Guo, J. Guo, C. Wang, G. Xu, X. Wu, G. Chen, J. Zhou, *Energy Environ. Sci.* **2020**, *13*, 503.
[31] Q. Zhang, J. Luan, X. Huang, Q. Wang, D. Sun, Y. Tang, X. Ji, H. Wang, *Nat. Commun.* **2020**, *586*, E11.
[32] D. Wang, D. Lv, H. Liu, S. Zhang, C. Wang, C. Wang, J. Yang, Y. Qian, *Angew. Chem., Int. Ed.* **2022**, *61*.
[33] D. Xie, Y. Sang, D. H. Wang, W. Y. Diao, F. Y. Tao, C. Liu, J. W. Wang, H. Z. Sun, J. P. Zhang, X. L. Wu, *Angew. Chem., Int. Ed.* **2023**, *62*, 202216934.
[34] Q. Zhang, Y. Ma, Y. Lu, Y. Ni, L. Lin, Z. Hao, Z. Yan, Q. Zhao, J. Chen, *J. Am. Chem. Soc.* **2022**, *144*, 18435.
[35] H. Tian, J. L. Yang, Y. Deng, W. Tang, R. Liu, C. Xu, P. Han, H. J. Fan, *Adv. Energy Mater.* **2023**, *13*, 2202603.
[36] K. Zhao, G. Fan, J. Liu, F. Liu, J. Li, X. Zhou, Y. Ni, M. Yu, Y. M. Zhang, H. Su, Q. Liu, F. Cheng, *J. Am. Chem. Soc.* **2022**, *144*, 11129.
[37] Z. Liu, R. Wang, Q. Ma, J. Wan, S. Zhang, L. Zhang, H. Li, Q. Luo, J. Wu, T. Zhou, J. Mao, L. Zhang, C. Zhang, Z. Guo, *Adv. Funct. Mater.* **2023**, *34*, 2214538.
[38] Z. Miao, Q. Liu, W. Wei, X. Zhao, M. Du, H. Li, F. Zhang, M. Hao, Z. Cui, Y. Sang, X. Wang, H. Liu, S. Wang, *Nano Energy* **2022**, *97*, 107145.
[39] M. Luo, C. Wang, H. Lu, Y. Lu, B. Bin Xu, W. Sun, H. Pan, M. Yan, Y. Jiang, *Energy Storage Mater.* **2021**, *41*, 515.
[40] L. Qian, W. Yao, R. Yao, Y. Sui, H. Zhu, F. Wang, J. Zhao, C. Zhi, C. Yang, *Adv. Funct. Mater.* **2021**, *31*, 2105736.
[41] T. Miyake, M. Rolandi, *J. Phys.: Condens. Matter* **2016**, *28*, 023001.
[42] H. Du, K. Wang, T. Sun, J. Shi, X. Zhou, W. Cai, Z. Tao, *Chem. Eng. J.* **2022**, *427*, 131705.
[43] Y. Sun, Z. Xu, X. Xu, Y. Nie, J. Tu, A. Zhou, J. Zhang, L. Qiu, F. Chen, J. Xie, T. Zhu, X. Zhao, *Energy Storage Mater.* **2022**, *48*, 192.
[44] J. Zheng, Q. Zhao, T. Tang, J. Yin, C. D. Quilty, G. D. Renderos, X. Liu, Y. Deng, L. Wang, D. C. Bock, C. Jaye, D. Zhang, E. S. Takeuchi, K. J. Takeuchi, A. C. Marschilok, L. A. Archer, *Science* **2019**, *366*, 645.
[45] X. Wang, J. Meng, X. Lin, Y. Yang, S. Zhou, Y. Wang, A. Pan, *Adv. Funct. Mater.* **2021**, *31*, 2106114.
[46] H. Fu, L. Xiong, W. Han, M. Wang, Y. J. Kim, X. Li, W. Yang, G. Liu, *Energy Storage Mater.* **2022**, *51*, 550.
[47] L. Kabalan, I. Kowalec, C. Richard, A. Catlow, A. J. Logsdail, *Phys. Chem. Chem. Phys.* **2021**,*23*, 14649.
[48] D. Wang, Q. Li, Y. Zhao, H. Hong, H. Li, Z. Huang, G. Liang, Q. Yang, C. Zhi, *Adv. Energy Mater* **2022**, *12*, 2102707.
[49] A. J. Bard, L. R. Faulkner, *Electrochemical methods : fundamentals and applications*, John Wiley and Sons, Hoboken, New Jersey **2000**.
[50] Y. Liu, X. Xu, M. Sadd, O. O. Kapitanova, V. A. Krivchenko, J. Ban, J. Wang, X. Jiao, Z. Song, J. Song, S. Xiong, A. Matic, *Adv. Sci.* **2021**, *8*, 2003301.
[51] P. Bai, J. Li, F. R. Brushett, M. Z. Bazant, *Energy Environ. Sci.* **2016**, *9*, 3221.
[52] K. Roy, A. Rana, J. N. Heil, B. M. Tackett, J. E. Dick, *Angew. Chem., Int. Ed.* **2024**, 202319010. https://doi.org/10.1002/anie.202319010.
[53] C. C. Kao, C. Ye, J. Hao, J. Shan, H. Li, S. Z. Qiao, *ACS Nano* **2023**, *17*, 3948.
[54] Z. Chen, C. Li, Q. Yang, D. Wang, X. Li, Z. Huang, G. Liang, A. Chen, C. Zhi, *Adv. Mater.* **2021**, *33*, 2105426.
[55] L. Ma, Q. Li, Y. Ying, F. Ma, S. Chen, Y. Li, H. Huang, C. Zhi, *Adv. Mater.* **2021**, *33*, 2007406.
[56] B. M. Tackett, D. Raciti, A. R. Hight Walker, T. P. Moffat, *J. Phys. Chem. Lett.* **2021**, *12*, 10936.
[57] D. B. Trimarco, S. B. Scott, A. H. Thilsted, J. Y. Pan, T. Pedersen, O. Hansen, I. Chorkendorff, P. C. K. Vesborg, *Electrochim. Acta* **2018**, *268*, 520.
[58] A. Pei, G. Zheng, F. Shi, Y. Li, Y. Cui, *Nano Lett.* **2017**, *17*, 1132.
[59] S. Bhoyate, S. Mhin, S. Mhin, J. E. Jeon, K. Park, J. Kim, W. Choi, W. Choi, *ACS Appl. Mater. Interfaces* **2020**, *12*, 27249.
[60] P. Sayavong, W. Zhang, S. T. Oyakhire, D. T. Boyle, Y. Chen, S. C. Kim, R. A. Vilá, S. E. Holmes, M. S. Kim, S. F. Bent, Z. Bao, Y. Cui, *J. Am. Chem. Soc.* **2023**, *145*, 12342.
[61] S. Guo, L. Qin, T. Zhang, M. Zhou, J. Zhou, G. Fang, S. Liang, *Energy Storage Mater.* **2021**, *34*, 545.
[62] K. Zhao, F. Liu, G. Fan, J. Liu, M. Yu, Z. Yan, N. Zhang, F. Cheng, *ACS Appl. Mater. Interfaces* **2021**, *13*, 47650.